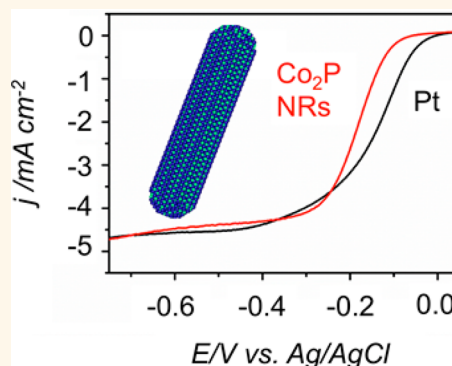# Synthesis and X-ray Characterization of Cobalt Phosphide (Co₂P) Nanorods for the Oxygen Reduction Reaction

Vicky V. T. Doan-Nguyen,[†] Sen Zhang,[‡] Edward B. Trigg,[†] Rahul Agarwal,[†] Jing Li,[§] Dong Su,[§] Karen I. Winey,[†] and Christopher B. Murray*,[†,‡]

[†]Department of Materials Science and Engineering, University of Pennsylvania, Philadelphia, Pennsylvania 19104, United States, [‡]Department of Chemistry, University of Pennsylvania, Philadelphia, Pennsylvania 19104, United States, and [§]Center for Functional Nanomaterials, Brookhaven National Laboratory, Upton, New York, New York 11973, United States

ABSTRACT Low temperature fuel cells are clean, effective alternative fuel conversion technology. Oxygen reduction reaction (ORR) at the fuel cell cathode has required Pt as the electrocatalyst for high activity and selectivity of the four-electron reaction pathway. Targeting a less expensive, earth abundant alternative, we have developed the synthesis of cobalt phosphide (Co₂P) nanorods for ORR. Characterization techniques that include total X-ray scattering and extended X-ray absorption fine structure revealed a deviation of the nanorods from bulk crystal structure with a contraction along the b orthorhombic lattice parameter. The carbon supported nanorods have comparable activity but are remarkably more stable than conventional Pt catalysts for the oxygen reduction reaction in alkaline environments.

Low temperature fuel cells have been actively investigated for five decades due to their appeal as a clean chemical-to-energy conversion technology.[1−4] Polymer electrolyte membrane fuel cells (PEMFCs) and alkaline fuel cells (AFCs) operate under 200 °C with desirable rapid start-up time and efficient conversion of H₂ and O₂ to H₂O and electricity. Fuel cell electrochemistry is predicated on the use of electrocatalysts at both cathode and anode to increase each half-cell reaction efficiency and selectivity. Platinum nanoparticles (NPs) with high surface area have proven to be robust electrocatalysts for both hydrogen oxidation and oxygen reduction reaction (ORR).[1,2,4,5] However, the high cost of Pt, approximately 50% of a fuel cell stack, has motivated many investigations to find less expensive, more earth abundant material alternatives for catalyzing either of the two half-reactions.[2,6−10] We focus on the cathode material because ORR still presents many serious commercialization challenges such as efficiency, materials cost, and stability. Even though many recent reports on nonprecious

metals,[11] metal−polymer composites,[12,13] and graphene-based systems[14−16] have shown promise in fabricating a catalyst beyond the Pt for ORR, it is still a challenge to provide a non-Pt-based catalyst with comparable or better activity, durability or selectivity to Pt catalysts.

Herein, we report a solution colloidal synthesis for cobalt phosphide (Co₂P) nanorods (NRs), which show promise as efficient catalysts for ORR in the alkaline solution. Controlled synthesis of 1D structured materials such as NRs is of great interest for many applications including optics,[17] electronics,[18] magnetism,[19,20] and catalysis.[21,22] In the colloidal solution chemistry, rod-like nanoparticles (NPs) can be produced by controlling surfactant choice and concentration,[23] time of growth,[24] and seeded precursors.[25−27] Previous studies have shown that, using trioctylphosphine and/or trioctylphosphine oxide as the phosphorus sources, metal nanoparticles (i.e., magnesium, nickel, iron, copper, molybdenum, palladium) can be converted to metal phosphides through the diffusion process resulting in hollowed

morphologies.[20,28−32] Co$_2$P NPs have been synthesized to support their applications in magnetics,[33] heterogeneous catalysis,[25,34−36] energy storage,[37,38] and heavy-metal capture and recycling.[39] Recently, cobalt phosphide (Co$_2$P NPs and CoP NRs) and other base-metal phosphides—synthesized *via* thermal decomposition in organic solvents—have also been reported to be excellent electrocatalysts for hydrogen evolution reaction (HER).[34,40,41] CoP NPs on glassy carbon are stable for up to 24 h for HER under strongly acidic conditions.[40] Co$_2$P NRs (≈ 7.5 nm × 120 nm) on glassy carbon have been shown to be HER electrocatalysts with comparable overpotential to that of Pt catalysts.[34] Such performance provides motivation for the study of ORR electrocatalysis by metal phosphide NPs.[26,40] Additionally, supported Fe$_2$P, Ni$_2$P, Co$_2$P, and CoP have been reported to be excellent catalysts for hydrodesulfurization (HDS) and hydrodenitrogenation (HDN) in addition to HER.[42−44] These supported catalysts were prepared with thermal decomposition of metal salt precursors in organic solvents[42] as well as wet impregnation on silica supports.[44] By using the cosurfactants of oleic acid (OLAC) and trioctylphosphine oxide (TOPO), we have synthesized monodisperse Co$_2$P NRs. The structure of the Co$_2$P NRs are systematically characterized by high-resolution transmission electron microscopy (HRTEM), high-angle annular dark field scanning transmission electron microscopy (HAADF-STEM), extended X-ray absorption fine structure spectroscopy (EXAFS), total X-ray scattering, and modeling using the Debye Equation. These techniques have been robust for not only distinguishing bimetallic core−shell *vs* alloy architectures but also to understand the formation of metal-oxide shells that emerge from cleaning pretreatments in preparation for functional testing.[45−48] Such careful study of the average and local crystallographic structures of our NRs provides valuable insights into the structure−property relations in shape-dependent electrocatalysis. Besides the unique 1-D structure, Co$_2$P NRs supported on carbon exhibit intriguing catalytic performance for catalyzing ORR in an alkaline medium. The Co$_2$P catalyst shows comparable activity and remarkable enhanced durability as compared to commercial Pt catalysts. This presents a new type of non-Pt containing electrocatalyst for ORR for alkaline fuel cells application.

RESULTS AND DISCUSSION

The morphology of the cobalt phosphide (Co$_2$P) NRs is dependent on the ligand concentration ratios of OLAC to TOPO as shown in the transmission electron microscopy (TEM) images of Figure 1. Use of 0.25 mol equiv of TOPO/Co(Ac$_2$) and 1 mol equiv of OLAC/Co(Ac$_2$) produced a mixture of spheres and rods. The reaction produced solely rods when the concentration of OLAC/Co(Ac$_2$) was increased to 3 molar equivalence. Further
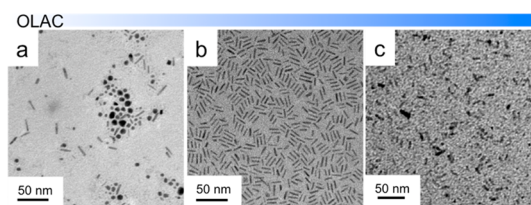

Figure 1. Transmission electron microscopy images of products synthesized with concentrations of oleic acid to trioctylphosphine oxide of (a) 1:0.25, (b) 3:0.25, and (c) 9:0.25.
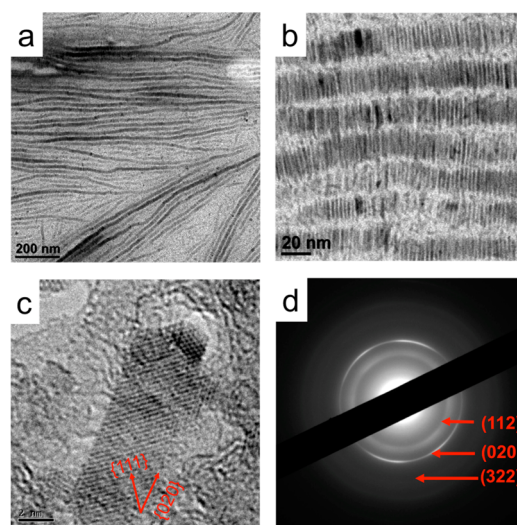

Figure 2. (a), (b) TEM images of aligned cobalt phosphide NRs at different magnifications. (c) High-resolution TEM and (d) electron diffraction of the NRs show growth along {020} direction.

increasing the amount OLAC to 9 mol equiv dramatically changes the growth kinetics and impedes nanorod formation. In addition, the evolution of nanoparticle morphology is dependent on the amount of TOPO present in the reaction since TOPO acts as the phosphorus source. Maintaining same molar equivalence of OLAC but increasing TOPO from 0.25 to 1 molar equivalence produced a similar mixture of rods and spheres (Figure S2). The costabilization of surfactants for selective binding to preferred crystal planes have been implemented for a variety of anisotropic morphologies among first-row transition metals and metal phosphides.[20,49] The morphology and dimensions were maintained when the reaction temperature was increased to 300 °C or when the time was increased from 60 to 120 min.

Nanorods have an average diameter of 2.8 ± 0.9 nm and an average length of 12.4 ± 3.5 nm based on TEM. The cooperative interplay between OLAC and TOPO resulted in anisotropic growth along the {020} direction of orthorhombic cobalt phosphide. The high-resolution (HRTEM) images shows a lattice spacing of 0.27 nm for the {111} direction and an interplanar angle of 39.2° between {020} and the {111} direction (Figure 2c). The small X-ray scattering (SAXS) pattern in
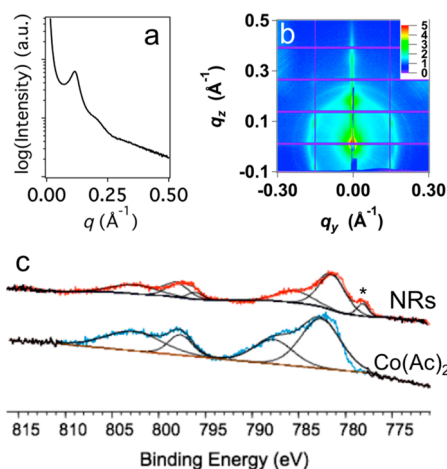
Figure 3. (a) SAXS of NRs, (b) GISAXS of Co$_2$P film on a silicon wafer, and (c) XPS shows the existence of oxidized and zerovalent states of cobalt. The minority metallic peak is denoted with an asterisk (*). The signal for cobalt acetate tetrahydrate precursor (blue) is shown for comparison with the NRs samples (red).

TABLE 1. Reflections for Cobalt Phosphide NRs and Miller Indices for the α-Co$_2$P Phase

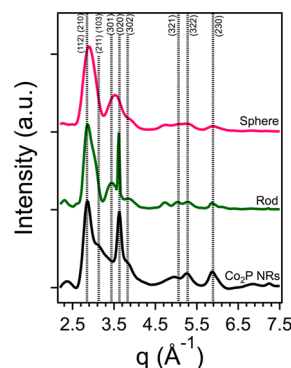| q (Å^{-1})	hkl
2.85	112, 210
3.10	211, 103
3.63	020
3.86	302
4.81	402
4.96	321
5.27	322
5.87	230

Figure 4. Experimental total X-ray scattering data is shown in black. Simulation of Co$_2$P NRs (green) confirms particle growth in the {020} direction and agrees with the experimental data as compared with a spherical model (pink). Both models were constructed from crystal structures with the contracted b lattice parameter. Dashed black lines have been drawn on the plot to help guide the eyes in tracing the hkl reflections.

Figure 3a confirms the nanorod self-assembly seen in Figure 2a,b with a peak at $q = 0.117$ Å^{-1}, corresponding to the expected average center-to-center distance of 2.8 ± 0.9 nm for the hard core surrounded by two layers of OLAC in the soft ligand shell.[50] Grazing incidence small-angle X-ray scattering of Co$_2$P showed that there is local hexagonal packing of the NRs in the films (Figure S3). This is based on higher scattering intensities at azimuthal angles of integer multiples of $\pi/3$ seen in Figure 3b. Out of the plane, nanorod films are oriented randomly as concluded by the constant intensities at a fixed scattering angle. Further confirmation of superlattice formation is provided in the TEM images in Figure S5 and S6.

The wide-angle X-ray scattering pattern was also simulated using the Debye equation, eq 1, to confirm the growth direction, calculate the size polydispersity, and quantify peak broadening from static and dynamic thermal motion. The intensity in the Debye Equation is the summation of the pairwise interactions at r_{ij} of atoms at each q (in which $q = 4\pi \sin \theta/\lambda$ for a scattering angle θ and at a wavelength of λ) and scaled by the atomic scattering factors of the ith and jth atoms (f_i and f_j if $i \neq j$).[51] This intensity is then damped by the Debye−Waller factor, B, representing the thermal motion of atoms at a given temperature, which was 25 °C. Here, B is equal to $8\pi^2\langle u^2\rangle$ in which u is the atomic displacement in Å. Size polydispersity was simulated as a Gaussian weighted average of the scattering from perfect crystals in which w_k is the normalized weighting factor.

$$I = \sum_k w_k \left(\exp\left(-\left(\frac{q}{4\pi}\right)^2 B \right) \sum_{i,j} f_i f_j \frac{\sin(qr_{ij})}{qr_{ij}} \right) \quad (1)$$

The q values for the NRs X-ray scattering pattern indexed for the Co$_2$P $Pnma$ are summarized in Table 1.

These ratios of the q values are in good agreement with the ratios of the lattice spacing as calculated from the selected area electron diffraction pattern (Figure 2d). When the lattice spacing from HRTEM is converted to q, the ratios are 1:1.28:1.86 as compared to the q values from electron diffraction, which are 1:1.27:1.85 for the (112), (020), and (322) peaks, respectively. Similar to structure refinement of bulk compounds of Co$_2$P (ICDD PDF No. 01−089−3030),[52] the scattering of nanocrystalline α-Co$_2$P captures the dominant (112) reflection at 2.85 Å^{-1} followed by the (103) reflection at 3.10 Å^{-1}. Additional reflections at $q = 3.63, 3.86, 4.81, 4.96, 5.27,$ and 5.87 Å^{-1} have been assigned to the (020), (302), (402), (321), (322) and (230) planes, respectively. These prominent reflections are only partially reproduced in a simulated Co$_2$P sphere with a radius of 2.8 nm using the Debye equation, Figure 4. The finite size effect broadening of the first peak results in indiscernible peak centers of the (112) and (201) reflections. The spherical model does not capture the high intensity of the (020) reflection. Overall, the scattering peaks from the spherical model are uniformly broadened as compared to peaks from NRs with a range of aspect ratios (Figure S4). Notably, the anisotropy of the NRs is evident in the high intensity and small width of the

(020) peak at $q = 3.63$ Å^{-1}. The 0.1 Å^{-1} shift in the NR model (Figure 4 green line) peak $q = 3.63$ Å^{-1} from the experimental data can be reasoned to originate from a 1% contraction in the b lattice parameter of the bulk orthorhombic crystal structure. The shift is not purely from the difference in the shape factor between a sphere and a rod with aspect ratio of 4.3. Bulk lattice parameters for Co$_2$P has been reported to be $a = 5.646$ Å, $b = 3.513$ Å, and $c = 6.608$ Å by S. Rundqvist with the atomic positions listed in Table S1.[52] Contraction of the b lattice parameters resulted in the (020) reflection shift in q while the dominant (112), (210) and (230) peak centers are maintained.

XPS (Figure 3c) confirmed the oxidized state of the cobalt species, with the detection of a binding energy of 781.7 eV.[53−55] In addition to the expected Co(II) state, zerovalent cobalt was also detected at 778.3 eV in sparse amounts due to trace amounts of amorphous cobalt present in the sample. The survey data collection with Gaussian fits resulted in 20.22% of O 1s, 73.57% of C 1s, 2.23% of P 2p and 3.98% of Co 2p. For Co 2p, elemental Co is 8.5% of the overall 3.98 or 0.34% of the total atomic percent with the balance of the Co 2p peaks being oxidized cobalt. The Co 2p$_{1/2}$ peak for the Co(II) species is seen at 797.9 eV with its shakeup satellite at 803.1 eV. In contrast to the NRs sample, only the Co(II) species was observed in the precursor for the Co 2p$_{3/2}$ peak at 782.7 eV. The peak shoulder occurring at 787.6 eV is a shakeup satellite peak arising from multiplet splitting of Co 2p$_{3/2}$. Additional peaks from the precursor sample for the Co(II) species can be seen in the Co 2p$_{1/2}$ peak at 797.8 eV and its satellite at 802.9 eV.

EXAFS captured the Co−P and Co−Co local environments of the cobalt phosphide phases. In the Co$_2$P first shell, the cobalt K-edge probes the photoelectron interaction from two types of cobalt atoms. To distinguish between the two sites, the atoms will be denoted as Co$_I$ and Co$_{II}$. The R_{eff} values and degeneracy for the path lengths are provided in Table S2 with the undistorted path lengths for bulk Co$_2$P in Table S3. In fitting the first shell in the Fourier transform of the k^3-weighted $\chi(k)$, the nearest neighbor phosphorus and cobalt scattering paths in the Co$_2$P were used. For a pure Co$_2$P, the short-range order consists of two peaks between 1 and 2 Å in the Fourier transform of the k-weighted EXAFS equation. However, the existence of the CoO and Co$_2$P broadened the signal and the Co−O and Co−P peaks are convoluted into one peak between 1 and 2 Å. Shown in Figure 5, the fit shows good agreement with the $\chi(R)$ with an R-factor of 9.648×10^{-3} and reduced χ^2 value of 25.057. Fitting the Fourier transformed EXAFS signal using bulk Co−P and Co−O distances was worse, resulting in an R-factor of 1.559×10^{-2} and reduced χ^2 of 135.363. A detailed list of first shell Co−P and Co−Co degeneracies—constrained to the same values as that in the bulk
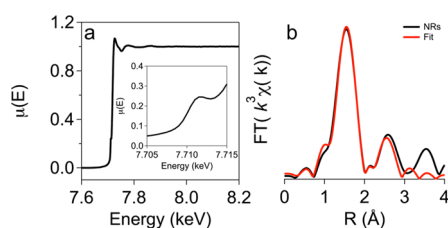

Figure 5. (a) EXAFS absorption with inset at the Co K-edge and (b) the Fourier transform, FT($k^3\chi(k)$), for Co$_2$P NRs. The data is shown in black, overlaid with the fit in red.

crystal structure—and half-path lengths are listed in Table S3. Additional fitting parameters are summarized in Table S4. To satisfy the Nyquist criteria for fitting k from 1.9 to 10 Å^{-1} with $dk = 1$ Å^{-1} and R from 1 to 3.4 Å, the amplitude and ΔE_0 were constrained for all Co−P and Co−Co scattering paths. The Co−O bond (with $Fm\bar{3}m$ symmetry) was constrained to the same S_0 with a separate ΔE_0. While the X-ray scattering did not detect Bragg diffraction from cobalt oxide phases as shown in Figure 4, the Co−O bonds were considered for the EXAFS fitting due to amorphous oxygen species on the surface of the cobalt NRs. The two Co$_I$−P and three Co$_{II}$−P paths were subsumed into one of each type for the EXAFS fitting due to the number of independent variable constraints as well as resolution from $\Delta k = 8.9$ Å^{-1}. Similar treatment was done for Co$_I$−Co and three Co$_{II}$−Co paths.

To study NRs electrocatalysis in ORR, we prepared the NR catalyst by loading the NRs on Ketjan carbon (C) with a weight ratio of 1:1 (NR: C) through sonication in hexane and activated the catalysts via thermal annealing at 180 °C and under the ambient pressure (metal weight percentage in NR-C composite is measured to be 20−22% by ICP). We further characterized the activated electrocatalyst with aberration-corrected STEM. Figure S7a is a HAADF-STEM image of the activated NRs on C, which shows the NRs are uniformly deposited on C and preserved their 1-D morphology after thermal treatment. STEM electron energy-loss (EELS) elemental mapping confirmed the phosphide and oxidized structure with Co, P, and O shown in Figure S7b−f. ORR polarization curves in Figure 6a indicate that Co$_2$P NRs/C has a steeper polarization curve and with a similar limit current density as compared to commercial Pt/C catalysts in the O$_2$-saturated 0.1 M KOH. Moreover, the Co$_2$P NRs/C catalyst has a half-wave potential at −0.196 V, which is only 49 mV below that of a commercial Pt catalyst. This suggests that the Co$_2$P's ORR catalytic activity performance is close to commercial Pt/C. It is noteworthy that the Co$_2$P NRs are supported on commercial carbon. Unlike systems using nanotubes, reduced graphene oxide, or highly ordered porous carbon matrices,[56] these NRs do not rely on the electrocatalytic activity enhancement from carbon support with such specific architectures.[57,58] Additionally, amorphous commercial carbon has the

benefit of being less expensive than the aforementioned support alternatives.

The ORR kinetics on Co_2P NRs were also evaluated using a range of controlled rotation speeds (Figure 6b) and the Koutecky−Levich Equation. As shown in Figure 6c, the linearity of the Koutecky−Levich plots and the parallelism of the fitting line suggest the first order reaction kinetics toward the concentration of O_2 on Co_2P NRs from −0.3 V to −0.75 V. The electron transfer number (n) was also calculated from the slopes of Koutecky−Levich plots according to the following equations.

$$\frac{1}{j} = \frac{1}{j_L} + \frac{1}{j_K} = \frac{1}{B\omega^2} + \frac{1}{j_K} \qquad (2)$$

$$B = 0.62nAFC_{O_2}D_{O_2}^{2/3}\nu^{-1/6} \qquad (3)$$

where j, j_K, and j_L are measured current, kinetic current and diffusion-limiting current respectively, ω is the angular velocity in radians/s, F is the Faraday constant (9.64853 $\times$ 10^4 C/mol), A is the electrode surface area in cm^2, C_{O_2} is the concentration of dissolved O_2 (1.26 $\times$ 10^{-6} mol/cm^3), D_{O_2} is the diffusion coefficient of O_2 (1.9 $\times$ 10^{-5} cm^2/s) and ν is the kinetic viscosity of the electrolyte (0.01 cm^2/s). Reconfiguring eq 3, n for Co_2P NRs is calculated to be 3.98−4.18. This was indicative of a complete four electron oxygen reduction process confirming the NRs' favorable kinetics for ORR, thus bypassing hydrogen peroxide production.

As reported from previous work on FePt-based nanowires and nanorods, 1-D structures showed stronger interaction with carbon support, thus allowing for higher stability than 0-D NPs in the catalysis.[59−61] Our Co_2P NRs/C catalyst also takes advantage of this strong interaction induced by 1-D shape to enhance its durability in catalyzing ORR. The catalyst's durability was performed using choronoamperometric testing at a voltage of −0.2 V in O_2-saturated 0.1 M KOH. As shown in Figure 6d, our Co_2P NRs/C catalyst showed a much slower current decay than the commercial Pt/C catalyst. After a 25 000-s test, the NRs/C catalyst retained a 75% of the original current density, while commercial Pt/C catalyst preserved only 48% of initial current density. The HAADF-STEM image of a large area of the Co_2P NRs/C catalyst in Figure 7a confirms that the NR morphology is maintained after stability testing. Additionally, the STEM-EELS line scan (Figure 7b) across a NR confirms the expected presence of Co, O, and P species. It is also clearly seen in both the HAADF-STEM image and STEM-EELS line scan that the core/shell structured Co_2P/CoO nanorods show no morphological change after electrocatalytic testing. The microscopy is in agreement with XPS data (Figure 7c), which does not show a change in the Co 2p peaks post electrocatalysis. Moreover, the choronoamperometric current of Co_2P NRs/C catalyst showed no obvious change upon the addition of 2 M methanol into the electrolyte, while the commercial Pt/C catalyst showed a current jump in the same condition due to methanol oxidation reaction (Figure S8). All these suggest much enhanced long-term stability and selectivity of Co_2P NRs over the commercial Pt catalysts for ORR.
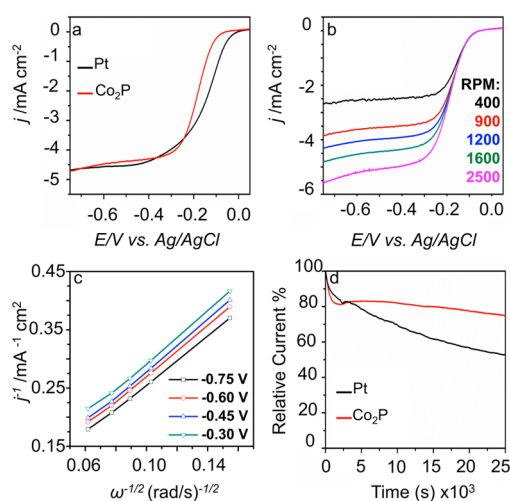

Figure 6. (a) ORR polarization curves of Co_2P NRs supported on Ketjan carbon as compared to commercial Pt at 1600 rpm, (b) ORR polarization curves of Co_2P NRs over a range of rotation speeds. Polarization measurements were performed in an O_2 saturated 0.1 M KOH solution. (c) Koutecky−Levich plots of Co_2P catalysts and (d) chronoamperometric response of Co_2P NR catalyst as compared to commercial Pt at −0.2 V in the O_2 saturated 0.1 M KOH solution.
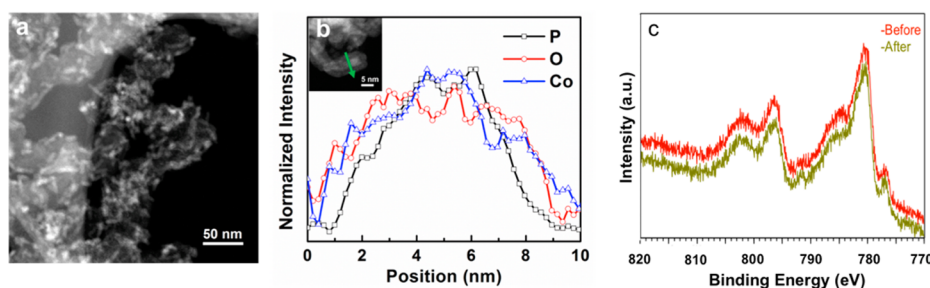

Figure 7. (a) STEM-HAADF image of the Co_2P NRs/C catalyst after the electrochemical stability test. (b) STEM-EELS line scan on a representative NRs after electrochemical stability testing. The inset image depicts the NR scanned. (c) XPS shows that the catalyst retains the same composition after electrocatalysis.

CONCLUSION

We have presented a one-pot synthesis of Co$_2$P NRs, which can be used as a new form of non-Pt electrocatalyst for ORR in the alkaline solution. The monodispersity in size and shape of the NRs was controlled by varying cosurfactant concentrations of oleic acid and trioctylphosphine oxide. Structural characterization involving electron microscopy, electron diffraction, total X-ray scattering, and EXAFS have confirmed the anisotropic growth of Co$_2$P particles in the {020} direction with thin amorphous CoO shell. Modeling demonstrated that there is a 1% contraction in the *b* lattice parameter of the orthorhombic crystal structure. Co$_2$P NR catalysts exhibited comparable ORR catalytic activity with superior durability in an alkaline solution as compared to commercial Pt catalysts. This is encouraging for use of Co$_2$P NR catalysts as an alternative to Pt catalysts for ORR.

EXPERIMENTAL SECTION.

Chemicals. Cobalt(II) acetate tetrahydrate (Co(Ac)$_2$), trioctylphosphine oxide (TOPO), tributylphosphine (97%) (TBP), oleic acid (OLAC), benzyl ether were purchased from Sigma-Aldrich and used without further purification.

Synthesis and Purification. Synthesis of NPs involves Schlenk line techniques that utilized thermal decomposition of a metalsalt precursor in a flask with surfactants and a high-boiling solvent. In a typical reaction, 1 mmol Co(Ac)$_2$, 1 mmol TOPO, and 3 mmol OLAC were loaded into a three-neck 50 mL flask containing 20 mL benzyl ether. The flask was degassed at 100 °C for 30 min. The flask was refilled with nitrogen. The solution temperature was increased to 200 °C at which point 3 mmol TBP was injected. Then, the reaction was carried out at 260 °C for 60 min. The reaction was air cooled to room temperature and washed with acetone and toluene. The solution was then centrifuged at 7000 rpm. The NRs were redispersed in toluene and washed again with acetone. After centrifugation at 7000 rpm, the NRs were collected and redispersed in hexane.

Characterization. For electron microscopy, the NPs were deposited on 300-mesh carbon-coated copper grids purchased from Electron Microscopy Sciences as well as holey carbon 400-mesh copper grids purchased from Ted Pella, Inc. TEM was done on a JEOL 1400 TEM with a LaB$_6$ filament, operating at 120 kV and equipped with an SC1000 ORIUS CCD camera and Digital Micrograph software. High-resolution TEM was done on a JEOL 2100 with a LaB$_6$ filament at 200 kV. Aberration-corrected HAADF-STEM imaging and STEM-EELS were performed at Brookhaven National Laboratory Center for Functional Nanomaterials on a Hitachi HD2700C at 200 kV with a Gatan Enfina-ER spectrometer.

X-ray photoelectron spectroscopy (XPS) was done on a Physical Electronics VersaProbe 5000. Analysis was made with High Power X-ray setting of 100 μm 25W electron beam. Photoelectrons were collected using hemispherical analyzer. Survey data collection was performed at 117 V. The powder samples were mounted onto the holder using double-sided tape. High-resolution spectra were calibrated using the C 1s line at 285 eV. High-resolution X-ray diffraction was done at Advanced Photon Source (APS) 11-ID-B at Argonne National Laboratory with 58.6 keV beam corresponding to a wavelength of 0.2114 Å. Background contributions from the Kapton capillary tape and poly(vinyl) butyral matrix were subtracted from the data. Simulation of the wide-angle X-ray diffraction pattern was done using an in-house Python script, which is available on Github.[62] The lattice parameters used in the X-ray simulation are as follows: $a = 5.646$ Å, $b = 3.478$ Å, and $c = 6.608$ Å.

Extended X-ray absorption fine structure (EXAFS) was done at APS 12-BM-B. The nanoparticle samples were loaded into a 1.5 mm Kapton tube for measurement. The absorption was measured from the cobalt *K*-edge (7.7 keV) and calibrated by normalization of the pre-edge and postedge from cobalt foil. The E_0 value from cobalt foil reference was used for all samples. The edge was set to 7.708 keV in accordance with Kraft *et al.*[63] Three fluorescence scans were averaged for the reported absorption intensity using ATHENA, an open source package for spectroscopy analysis.[64] Analysis was done during the *ab initio* package ARTEMIS[64] between 1 and 3 Å, and structure models were created using ATOMS.[65] The same unit cell used in X-ray fitting was used for EXAFS fitting in which only the *b* lattice parameter was contracted by 1%. The *k* range was analyzed from 1.9 to 10 Å^{-1} with Hanning windows and sills of 1 Å^{-1}. GISAXS was done APS 12-ID-B. The scattered photons from 1-s exposures were collected using a Pilatus 2 M area detector positioned at 2 m from the sample. The incident angles of the 14 keV (0.886 Å) X-ray beam ranged from 0.02 to 0.15. The standard used for *q* calibration was silver behenate. Data reduction was performed using computer program GISAXShop.

Oxygen reduction reaction electrocatalysis testing was done using a glassy carbon rotating disk electrode on the Bioanalytical Systems, Inc. Epsilon potentiostat. Voltage values for commercial Pt purchased from the Fuel Cells Store and Co$_2$P NRs were normalized against a Ag/AgCl reference electrode (3 M NaCl) and Pt coil as the counter electrode. Two mg/mL NRs/C catalyst ink was made by dispersing catalyst in the mixture of deionized water and isopropanol (IPA) in a volume ratio of 4:1 H$_2$O:IPA and 0.5% Nafion. Twenty μL catalyst ink was then transferred onto the glassy carbon RDE of 6 mm diameter and dried in the ambient condition. Similar sample preparation was done for commercial 2.5−3.5 nm Pt on carbon. ORR polarization measurements were collected using linear scan voltammetry (10 mV/s) with rotation speeds of 400, 900, 1200, 1600, and 2500 rpm. Both polarization measurements and stability testing was done in an O$_2$-saturated 0.1 M KOH solution. Stability tests were performed by recording the chronoamperometric response of catalyst at −0.2 V and with a rotation speed of 200 rpm for total of 25 000 s. Following the stability test, the methanol poisoning tests were performed by injecting 2 M methanol into O$_2$-saturated 0.1 M KOH at −0.2 V during chronoamperometry measurement.

Conflict of Interest: The authors declare no competing financial interest.

Supporting Information Available: Detailed information regarding size distribution of nanorods, X-ray modeling, and

REFERENCES AND NOTES

1. Jaouen, F.; Proietti, E.; Lefèvre, M.; Chenitz, R.; Dodelet, J.-P.; Wu, G.; Chung, H. T.; Johnston, C. M.; Zelenay, P. Recent Advances in Non-Precious Metal Catalysis for Oxygen-Reduction Reaction in Polymer Electrolyte Fuel Cells. *Energy Environ. Sci.* **2011**, *4*, 114.

2. Markovic, N. M.; Schmidt, T. J.; Stamenkovic, V.; Ross, P. N. Oxygen Reduction Reaction on Pt and Pt Bimetallic Surfaces: A Selective Review. *Fuel Cells* **2001**, *1*, 105–116.

3. *Basic Research Needs for the Hydrogen Economy*; U.S. Department of Energy: Washington, D.C., 2003.

4. *Fuel Cell Handbook*; EG&G Technical Services, Inc.: San Francisco, CA, 2004.

5. Guo, S.; Zhang, S.; Sun, S. Tuning Nanoparticle Catalysis for the Oxygen Reduction Reaction. *Angew. Chem., Int. Ed.* **2013**, *52*, 8526–8544.

6. Stamenkovic, V. R.; Fowler, B.; Mun, B. S.; Wang, G.; Ross, P. N.; Lucas, C. A.; Marković, N. M. Improved Oxygen Reduction Activity on Pt₃Ni(111) *via* Increased Surface Site Availability. *Science* **2007**, *315*, 493–497.

7. Lim, B.; Jiang, M.; Camargo, P. H. C.; Cho, E. C.; Tao, J.; Lu, X.; Zhu, Y.; Xia, Y. Pd-Pt Bimetallic Nanodendrites with High Activity for Oxygen Reduction. *Science* **2009**, *324*, 1302–1305.

8. Toda, T.; Igarashi, H.; Uchida, H.; Watanabe, M. Enhancement of the Electroreduction of Oxygen on Pt Alloys with Fe, Ni, and Co. *J. Electrochem. Soc.* **1999**, *146*, 3750–3756.

9. Mukerjee, S.; Srinivasan, S.; Soriaga, M. P.; McBreen, J. Role of Structural and Electronic Properties of Pt and Pt Alloys on Electrocatalysis of Oxygen Reduction. *J. Electrochem. Soc.* **1995**, *142*, 1409–1422.

10. Paulus, U. A.; Wokaun, A.; Scherer, G. G. Oxygen Reduction on Carbon-Supported Pt - Ni and Pt - Co Alloy Catalysts. *J. Phys. Chem. B* **2002**, *106*, 4181–4191.

11. Chen, Z.; Higgins, D.; Yu, A.; Zhang, L.; Zhang, J. A Review on Non-Precious Metal Electrocatalysts for PEM Fuel Cells. *Energy Environ. Sci.* **2011**, *4*, 3167.

12. Bashyam, R.; Zelenay, P. A Class of Non-Precious Metal Composite Catalysts for Fuel Cells. *Nature* **2006**, *443*, 63–66.

13. Nallathambi, V.; Lee, J.-W.; Kumaraguru, S. P.; Wu, G.; Popov, B. N. Development of High Performance Carbon Composite Catalyst for Oxygen Reduction Reaction in PEM Proton Exchange Membrane Fuel Cells. *J. Power Sources* **2008**, *183*, 34–42.

14. Qu, L.; Liu, Y.; Baek, J. B.; Dai, L. Nitrogen-Doped Graphene as Efficient Metal-Free Electrocatalyst for Oxygen Reduction in Fuel Cells. *ACS Nano* **2010**, *4*, 1321–1326.

15. Yang, S.; Feng, X.; Wang, X.; Müllen, K. Graphene-Based Carbon Nitride Nanosheets as Efficient Metal-Free Electrocatalysts for Oxygen Reduction Reactions. *Angew. Chem., Int. Ed.* **2011**, *50*, 5339–5343.

16. Geng, D.; Chen, Y.; Chen, Y.; Li, Y.; Li, R.; Sun, X.; Ye, S.; Knights, S. High Oxygen-Reduction Activity and Durability of Nitrogen-Doped Graphene. *Energy Environ. Sci.* **2011**, *4*, 760.

17. Ye, X.; Jin, L.; Caglayan, H.; Chen, J.; Xing, G.; Zheng, C.; Doan-Nguyen, V.; Kang, Y.; Engheta, N.; Kagan, C. R.; *et al.* Improved Size-Tunable Synthesis of Monodisperse Gold Nanorods through the Use of Aromatic Additives. *ACS Nano* **2012**, *6*, 2804–2817.

18. Spurgeon, J. M.; Atwater, H. A.; Lewis, N. S. A Comparison Between the Behavior of Nanorod Array and Planar Cd(Se, Te). *J. Phys. Chem. C* **2008**, *112*, 6186–6193.

19. Cordente, N.; Respaud, M.; Senocq, F.; Casanove, M.-J.; Amiens, C.; Chaudret, B. Synthesis and Magnetic Properties of Nickel Nanorods. *Nano Lett.* **2001**, *1*, 565–568.

20. Park, J.; Koo, B.; Hwang, Y.; Bae, C.; An, K.; Park, J.-G.; Park, H. M.; Hyeon, T. Novel Synthesis of Magnetic Fe₂P Nanorods from Thermal Decomposition of Continuously Delivered Precursors Using a Syringe Pump. *Angew. Chem., Int. Ed.* **2004**, *43*, 2282–2285.

21. Xie, X.; Li, Y.; Liu, Z.; Haruta, M.; Shen, W. Low-Temperature Oxidation of CO Catalysed by Co₃O₄ Nanorods. *Nature* **2009**, *458*, 746–749.

22. Zhang, S.; Shan, J.; Zhu, Y.; Frenkel, A. I.; Patolla, A.; Huang, W.; Yoon, S. J.; Wang, L.; Yoshida, H.; Takeda, S.; *et al.* WGS Catalysis and *In Situ* Studies of CoO₁₋ₓ, PtCoₙ/Co₃O₄, and PtCoₘ/CoO₁₋ₓ Nanorod Catalysts. *J. Am. Chem. Soc.* **2013**, *135*, 8283–8293.

23. Qian, X. F.; Xie, Y.; Qian, Y. T.; Zhang, X. M.; Wang, W. Z.; Yang, L. Organo-Thermal Preparation of Nanocrystalline Cobalt Phosphides. *Mater. Sci. Eng., B* **1997**, *49*, 135–137.

24. Park, J. J.; Koo, B.; Yoon, K. Y.; Hwang, Y.; Kang, M.; Hyeon, T.; Park, J. J.; Hyeon, T. Generalized Synthesis of Metal Phosphide Nanorods *via* Thermal Decomposition of Continuously Delivered Metal-Phosphine Complexes Using a Syringe Pump. *J. Am. Chem. Soc.* **2005**, *127*, 8433–8440.

25. Ryu, J.; Jung, N.; Lim, D.-H.; Shin, D. Y.; Park, S. H.; Ham, H. C.; Jang, J. H.; Kim, H.-J.; Yoo, S. J. P-Modified and Carbon Shell Coated Co Nanoparticles for Efficient Alkaline Oxygen Reduction Catalysis. *Chem. Commun.* **2014**, *50*, 15940–15943.

26. Ha, D.-H.; Moreau, L. M.; Bealing, C. R.; Zhang, H.; Hennig, R. G.; Robinson, R. D. The Structural Evolution and Diffusion during the Chemical Transformation from Cobalt to Cobalt Phosphide Nanoparticles. *J. Mater. Chem.* **2011**, *21*, 11498–11510.

27. Lukehart, C. M.; Milne, S. B.; Stock, S. R. Formation of Crystalline Nanoclusters of Fe2P, RuP, Co2P, Rh2P, Ni2P, Pd₅P2, or PtP2 in a Silica Xerogel Matrix from Single-Source Molecular Precursors. *Chem. Mater.* **1998**, *10*, 903–908.

28. Wang, J.; Yang, Q.; Zhang, Z.; Sun, S. Phase-Controlled Synthesis of Transition-Metal Phosphide Nanowires by Ullmann-Type Reactions. *Chem. - Eur. J.* **2010**, *16*, 7916–7924.

29. Henkes, A. E.; Vasquez, Y.; Schaak, R. E. Converting Metals into Phosphides: A General Strategy for the Synthesis of Metal Phosphide Nanocrystals. *J. Am. Chem. Soc.* **2007**, *129*, 1–5.

30. Brock, S. L.; Perera, S. C.; Stamm, K. L. Chemical Routes for Production of Transition-Metal Phosphides on the Nanoscale: Implications for Advanced Magnetic and Catalytic Materials. *Chem. - Eur. J.* **2004**, *10*, 3364–3371.

31. Lo, C.-T.; Kuo, P.-Y. Synthesis and Magnetic Properties of Iron Phosphide Nanorods. *J. Phys. Chem. C* **2010**, *114*, 4808–4815.

32. Perera, S. C.; Tsoi, G.; Wenger, L. E.; Brock, S. L. Synthesis of MnP Nanocrystals by Treatment of Metal Carbonyl Complexes with Phosphines: A New, Versatile Route to Nanoscale Transition Metal Phosphides. *J. Am. Chem. Soc.* **2003**, *125*, 13960–13961.

33. Zhang, J.; Yan, Y.; Chen, J.; Chance, W. M.; Hayat, J.; Gai, Z.; Tang, C. Nanostructured Metal/Carbon Composites from Heterobimetallic Block Copolymers with Controlled Magnetic Properties. *Chem. Mater.* **2014**, *26*, 3185–3190.

34. Lu, A.; Chen, Y.; Li, H.; Dowd, A.; Cortie, M. B.; Xie, Q.; Guo, H.; Qi, Q.; Peng, D.-L. Magnetic Metal Phosphide Nanorods as Effective Hydrogen-Evolution Electrocatalysts. *Int. J. Hydrogen Energy* **2014**, *39*, 18919–18928.

35. Ni, Y.; Li, J.; Zhang, L.; Yang, S.; Wei, X. Urchin-like Co₂P Nanocrystals: Synthesis, Characterization, Influencing Factors and Photocatalytic Degradation Property. *Mater. Res. Bull.* **2009**, *44*, 1166–1172.

36. Tian, J.; Liu, Q.; Asiri, A. M.; Sun, X. Self-Supported Nanoporous Cobalt Phosphide Nanowire Arrays: An Efficient 3D Hydrogen-Evolving Cathode over the Wide Range of pH 0−14. *J. Am. Chem. Soc.* **2014**, *136*, 7587–7590.

37. Pralong, V.; Souza, D. C. S.; Leung, K. T.; Nazar, L. F. Reversible Lithium Uptake by CoP₃ at Low Potential: Role of the Anion. *Electrochem. Commun.* **2002**, *4*, 516–520.

38. Peng, W.; Jiao, L.; Huan, Q.; Li, L.; Yang, J.; Zhao, Q.; Wang, Q.; Du, H.; Liu, G.; Si, Y.; *et al.* Co₂P: A Facile Solid State Synthesis and Its Applications in Alkaline Rechargeable Batteries. *J. Alloys Compd.* **2012**, *511*, 198–201.

39. Yuan, F.; Ni, Y.; Zhang, L.; Ma, X.; Hong, J. Rod-Like Co₂P Nanostructures: Improved Synthesis, Catalytic Property

and Application in the Removal of Heavy Metal. *J. Cluster Sci.* **2013**, *24*, 1067–1080.

40. Popczun, E. J.; Read, C. G.; Roske, C. W.; Lewis, N. S.; Schaak, R. E. Highly Active Electrocatalysis of the Hydrogen Evolution Reaction by Cobalt Phosphide Nanoparticles. *Angew. Chem., Int. Ed.* **2014**, *53*, 5427–5430.

41. Popczun, E. J.; McKone, J. R.; Read, C. G.; Biacchi, A. J.; Wiltrout, A. M.; Lewis, N. S.; Schaak, R. E. Nanostructured Nickel Phosphide as an Electrocatalyst for the Hydrogen Evolution Reaction. *J. Am. Chem. Soc.* **2013**, *135*, 9267–9270.

42. Senevirathne, K.; Burns, a. W.; Bussell, M. E.; Brock, S. L. Synthesis and Characterization of Discrete Nickel Phosphide Nanoparticles: Effect of Surface Ligation Chemistry on Catalytic Hydrodesulfurization of Thiophene. *Adv. Funct. Mater.* **2007**, *17*, 3933–3939.

43. Oyama, S. T. Novel Catalysts for Advanced Hydroprocessing: Transition Metal Phosphides. *J. Catal.* **2003**, *216*, 343–352.

44. Cecilia, J. A.; Infantes-Molina, A.; Rodriguez-Castellon, E.; Jimenez-Lopez, A. The Influence of the Support on the Formation of Ni_2P Based Catalysts by a New Synthetic Approach. Study of the Catalytic Activity in the HDS of Dibenzothiophene. *J. Phys. Chem. C* **2009**, *113*, 17032–17044.

45. Alayoglu, S.; Zavalij, P.; Eichhorn, B.; Wang, Q.; Frenkel, A. I.; Chupas, P. Structural and Architectural Evaluation of Bimetallic Nanoparticles: A Case Study of Pt-Ru Core-Shell and Alloy Nanoparticles. *ACS Nano* **2009**, *3*, 3127–3137.

46. Sasaki, K.; Wang, J. X.; Naohara, H.; Marinkovic, N.; More, K.; Inada, H.; Adzic, R. R. Recent Advances in Platinum Monolayer Electrocatalysts for Oxygen Reduction Reaction: Scale-up Synthesis, Structure and Activity of Pt Shells on Pd Cores. *Electrochim. Acta* **2010**, *55*, 2645–2652.

47. Principi, E.; Witkowska, A.; Dsoke, S.; Marassi, R.; Di Cicco, A. An XAS Experimental Approach to Study Low Pt Content Electrocatalysts Operating in PEM Fuel Cells. *Phys. Chem. Chem. Phys.* **2009**, *11*, 9987–9995.

48. Alayoglu, S.; Nilekar, A. U.; Mavrikakis, M.; Eichhorn, B. Ru-Pt Core-Shell Nanoparticles for Preferential Oxidation of Carbon Monoxide in Hydrogen. *Nat. Mater.* **2008**, *7*, 333–338.

49. Puntes, V. F.; Krishnan, K. M.; Alivisatos, A. P. Colloidal Nanocrystal Shape and Size Control: The Case of Cobalt. *Science* **2001**, *291*, 2115–2117.

50. Pietra, F.; Rabouw, F. T.; Evers, W. H.; Byelov, D. V.; Petukhov, A. V.; de Mello Donegá, C.; Vanmaekelbergh, D. Semiconductor Nanorod Self-Assembly at the Liquid/Air Interface Studied by *In Situ* GISAXS and *Ex Situ* TEM. *Nano Lett.* **2012**, *12*, 5515–5523.

51. Debye, P. Zerstreuung von Röntgenstrahlen. *Ann. Phys.* **1915**, *351*, 809–823.

52. Rundqvist, S. The Structures of Co_2P, Ru_2P and Related Phases. *Acta Chem. Scand.* **1960**, *14*, 1961–1979.

53. Blanchard, P. E. R.; Grosvenor, A. P.; Cavell, R. G.; Mar, A. X-Ray Photoelectron and Absorption Spectroscopy of Metal-Rich Phosphides M_2P and M_3P (M=Cr−Ni). *Chem. Mater.* **2008**, *20*, 7081–7088.

54. Moulder, J. F.; Stickle, W. F.; Sobol, P. E.; Bomben, K. D. *Handbook of X-Ray Photoelectron Spectroscopy*; Chastain, J., King, R. C., Jr., Eds.; Physical Electronics, Inc.: Eden Prairie, MN, 1995.

55. Grosvenor, A. P.; Wik, S. D.; Cavell, R. G.; Mar, A. Examination of the Bonding in Binary Transition-Metal Monophosphides MP (M= Cr, Mn, Fe, Co) by X-Ray Photoelectron Spectroscopy. *Inorg. Chem.* **2005**, *44*, 8988–8998.

56. Xia, W.; Zou, R.; An, L.; Xia, D.; Guo, S. A Metal−organic Framework Route to *In Situ* Encapsulation of Co@Co_3O_4@C Core@bishell Nanoparticles into a Highly Ordered Porous Carbon Matrix for Oxygen Reduction. *Energy Environ. Sci.* **2015**, *8*, 568–576.

57. Liang, Y.; Li, Y.; Wang, H.; Zhou, J.; Wang, J.; Regier, T.; Dai, H. Co_3O_4 Nanocrystals on Graphene as a Synergistic Catalyst for Oxygen Reduction Reaction. *Nat. Mater.* **2011**, *10*, 780–786.

58. Guo, S.; Zhang, S.; Wu, L.; Sun, S. Co/CoO Nanoparticles Assembled on Graphene for Electrochemical Reduction of Oxygen. *Angew. Chem., Int. Ed.* **2012**, *51*, 11770–11773.

59. Guo, S.; Li, D.; Zhu, H.; Zhang, S.; Markovic, N. M.; Stamenkovic, V. R.; Sun, S. FePt and CoPt Nanowires as Efficient Catalysts for the Oxygen Reduction Reaction. *Angew. Chem., Int. Ed.* **2013**, *52*, 3465–3468.

60. Zhu, H.; Zhang, S.; Guo, S.; Su, D.; Sun, S. Synthetic Control of FePtM Nanorods (M = Cu, Ni) to Enhance the Oxygen Reduction Reaction. *J. Am. Chem. Soc.* **2013**, *135*, 7130–7133.

61. Guo, S.; Zhang, S.; Su, D.; Sun, S. Seed-Mediated Synthesis of Core/shell FePtM/FePt (M = Pd, Au) Nanowires and Their Electrocatalysis for Oxygen Reduction Reaction. *J. Am. Chem. Soc.* **2013**, *135*, 13879–13884.

62. Trigg, E. B. *DebyeByPy Github Repository*; https://github.com/etrigg/DebyeByPy.

63. Kraft, S.; Stümpel, J.; Becker, P.; Kuetgens, U. High Resolution X-Ray Absorption Spectroscopy with Absolute Energy Calibration for the Determination of Absorption Edge Energies. *Rev. Sci. Instrum.* **1996**, *67*, 681–687.

64. Ravel, B.; Newville, M. ATHENA, ARTEMIS, HEPHAESTUS: Data Analysis for X-Ray Absorption Spectroscopy Using IFEFFIT. *J. Synchrotron Radiat.* **2005**, *12*, 537–541.

65. Ravel, B. ATOMS: Crystallography for the X-Ray Absorption Spectroscopist. *J. Synchrotron Radiat.* **2001**, *8*, 314–316.